nature materials

SUPPLEMENTARY INFORMATION

https://doi.org/10.1038/s41563-018-0040-6

In the format provided by the authors and unedited.

# Electric-field switching of two-dimensional van der Waals magnets

**Shengwei Jiang[1,2], Jie Shan[1,2,3]* and Kin Fai Mak[1,2,3]***

[1]Department of Physics and School of Applied and Engineering Physics, Cornell University, Ithaca, NY, USA. [2]Department of Physics, The Pennsylvania State University, University Park, PA, USA. [3]Kavli Institute at Cornell for Nanoscale Science, Ithaca, NY, USA. *e-mail: jie.shan@cornell.edu; kinfai.mak@cornell.edu

# Supplementary Information for
# "Electric-field switching of two-dimensional van der Waals magnets"

Shengwei Jiang, Jie Shan*, and Kin Fai Mak*
*Correspondence to: jie.shan@cornell.edu, kinfai.mak@cornell.edu

## 1. Basic characterizations of bulk $CrI_3$ crystals

We have characterized bulk $CrI_3$ crystals (HQ Graphene) by both the Raman spectroscopy and Superconducting Quantum Interference Device (SQUID) magnetometry. Figure S1 (left panel) shows the Raman spectrum of bulk $CrI_3$ at 75 K (above the Curie temperature). The calculated phonon dispersion of bulk $CrI_3$ [1] is included in the right panel for comparison. Reasonable agreement is observed. Figure S2 is the magnetic-field dependence of the sample's magnetization measured by the SQUID magnetometry. The Curie temperature was determined to be 61.5 K from the peak of the temperature dependence of the magnetic susceptibility. Both the out-of-plane and in-plane dependences are included, showing the out-of-plane anisotropy of the material. The results are consistent with the reported ones [2, 3].

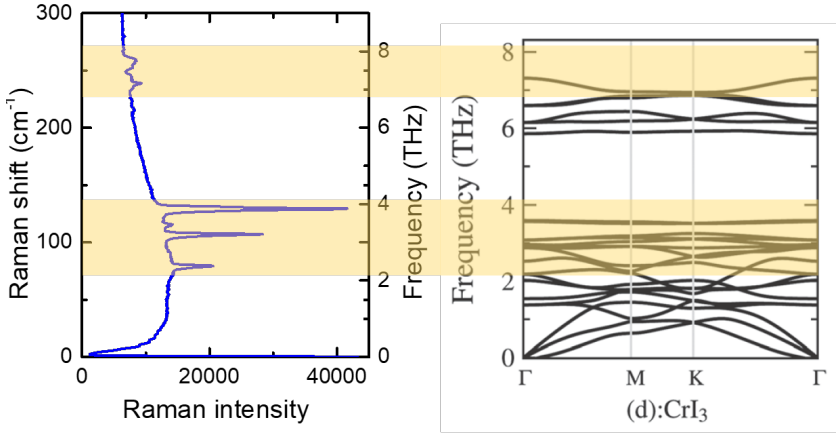


**Figure S1 |** Right: Raman spectrum of bulk $CrI_3$ in the paramagnetic phase (75 K). Left: the calculated phonon dispersion from ref. [1] for comparison.

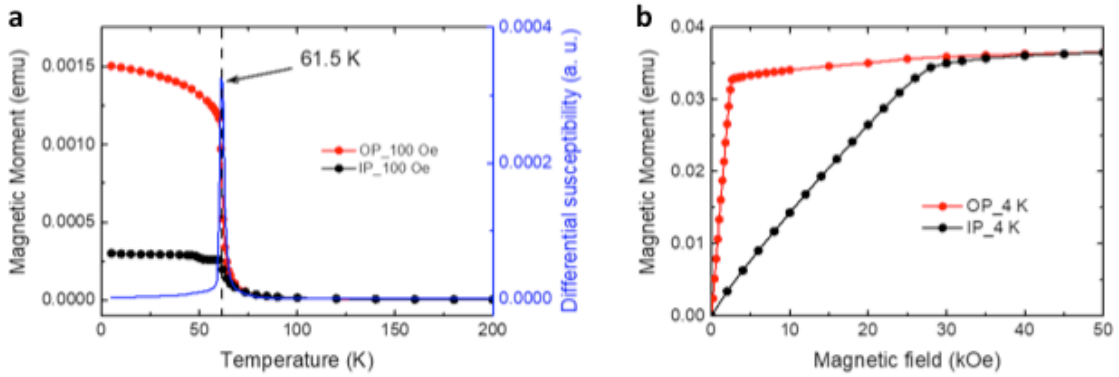


**Figure S2 | a,** Magnetization (left axis) as a function of temperature for bulk $CrI_3$ under both an out-of-plane (red) and in-plane (black) magnetic field of 100 Oe. The temperature dependence of the differential magnetic susceptibility (right axis) shows a sharp peak at the Curie temperature of 61.5 K. **b,** Magnetization as a function of out-of-plane (red) and in-plane (black) magnetic field at 4 K, demonstrating the out-of-plane anisotropy of the material.

## 2. Monolayer and bilayer $CrI_3$ samples and devices

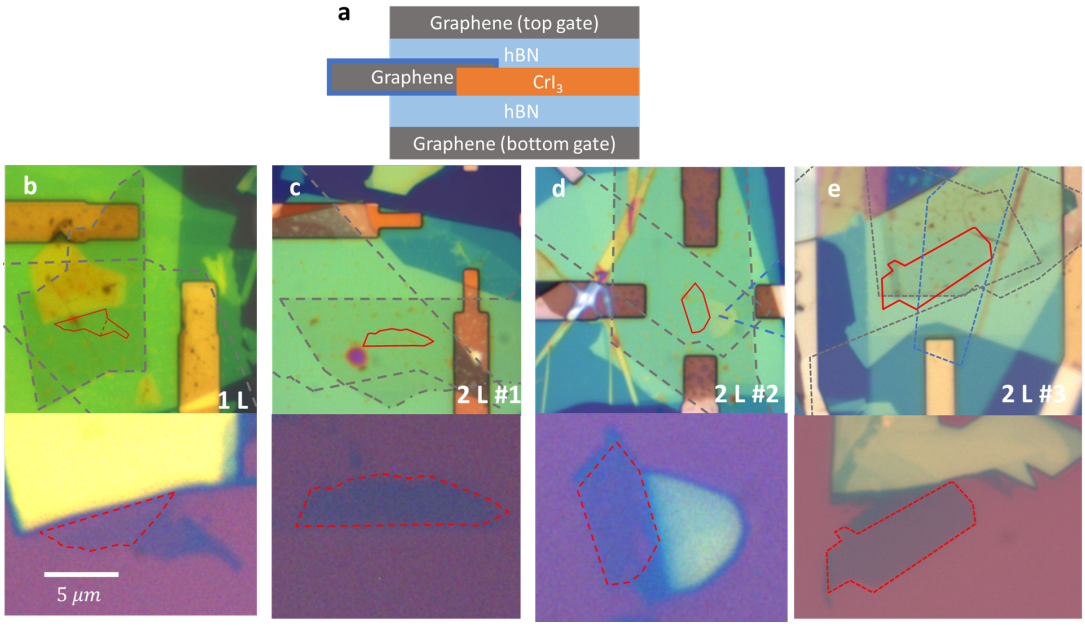


**Figure S3 | a**, Schematic cross section of dual-gate $CrI_3$ devices with graphene top and bottom gate electrodes and hexagonal boron nitride (hBN) gate dielectrics. The sample is also contacted by graphene. **b – e,** Top: optical microscope image of a monolayer (**b**) and three bilayer devices (**c – d**) on silicon substrates. The $CrI_3$ samples are fully encapsulated in hBN. The boundaries of the $CrI_3$ flakes and the graphene gates are shown in red and grey lines, respectively. Bottom: optical microscope images of $CrI_3$ samples before being encapsulated in hBN. The boundary of the samples is marked by red dashed lines.

## 3. Substrate effect on interlayer spin-flip transition

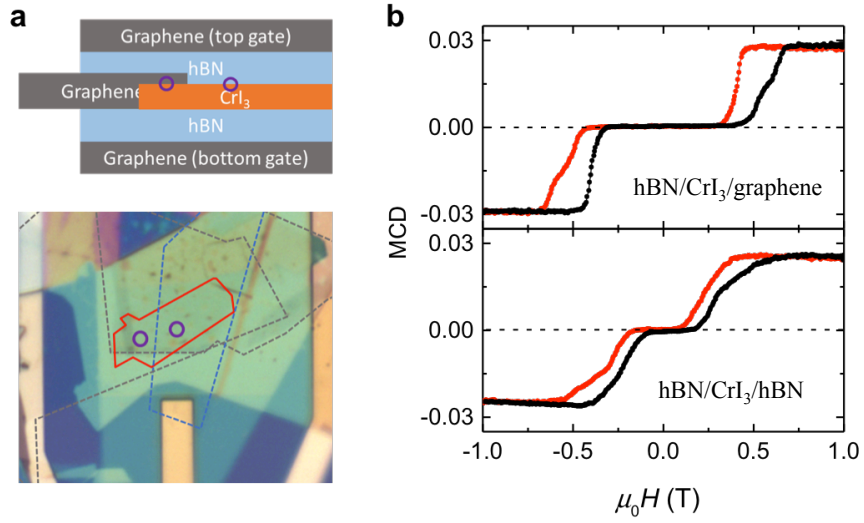


**Figure S4 | a,** Schematic side view (top) and optical micrograph (bottom) of a bilayer $CrI_3$ sample on hBN substrate on one side and partially covered by graphene and partially covered by hBN on the other side. **b,** Magnetic-field dependence of the MCD signal of two sample regions (marked by blue circles in **a**) corresponding to hBN/$CrI_3$/graphene (top) and hBN/$CrI_3$/hBN (bottom).

To examine the substrate effect on the spin-flip transition in bilayer $CrI_3$, we have studied a bilayer $CrI_3$ sample on an hBN substrate on one side and partially covered by

graphene and partially covered by hBN on the other side (Fig. S4a). Figure S4b shows the magnetic-field dependence of the magnetic circular dichroism (MCD) signal of these two different regions at 4 K near zero perpendicular electric field. The spin-flip transition is sharper and occurs at a higher magnetic field (~ 0.5 T) for hBN/$CrI_3$/graphene, which is comparable to that of Ref. [4]. We discuss the effect of domains and sample inhomogeneities on the transition width in Sect. 5. The microscopic origin of the substrate effect is unclear. It is likely related to charge transfer at the interfaces.

## 4. Determination of the critical field for the spin-flip transition

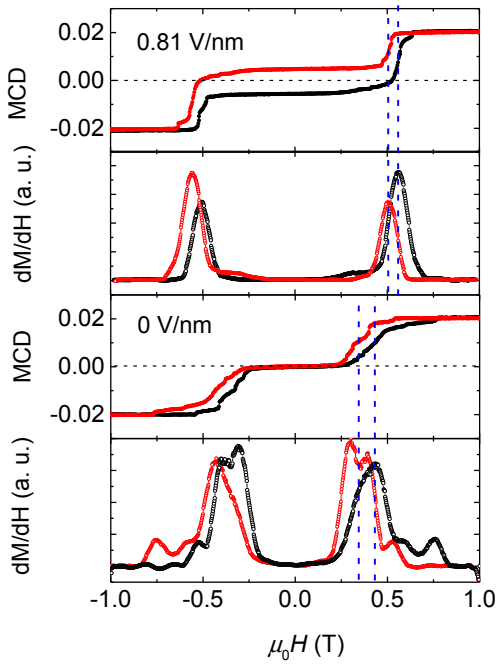


**Figure S5 |** Determination of the spin-flip critical field under two representative electric fields.

The critical magnetic field for the spin-flip transition was determined following the method described in Ref. [5]. Figure S5 illustrates two examples under electric fields at 0 V/nm and 0.81 V/nm. The differential magnetic susceptibility was first calculated numerically from the measured magnetic-field dependence of the magnetization (or MCD signal). The peak is defined as the critical field for the spin-flip transition (blue dash lines). The full-width-at-half-maximum (FWHM) of the peak was taken to be the transition width shown as the vertical bars in Fig. 1d and 2c of the main text.

## 5. Magnetic inhomogeneities across the spin-flip transition

Figure S6 shows the MCD images of bilayer $CrI_3$ under varying magnetic fields across the spin-flip transition. The electric field was fixed at 0.1 V/nm. The MCD images were obtained using broad field illumination with circularly polarized light at 632 nm. The images were calculated as the difference between the reflected left- and right-handed intensities normalized by the total reflected intensity. The spatial resolution (~ 500 nm) is diffraction limited. Small AFM and FM domains (corresponding to small and

large MCD signals) are visible near the spin-flip transition. The results suggest that the transition is inhomogeneously broadened, i.e. different locations of the sample have slightly different critical fields. The AFM-FM transition may involve nucleation of domains, domain wall motions and spin reorientation.

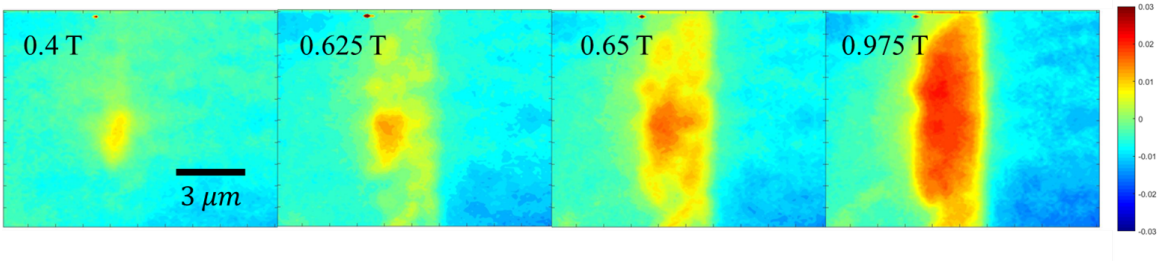


**Figure S6** | MCD images of bilayer $CrI_3$ (device #1) at varying magnetic fields across the spin-flip transition. The vertical electric field was kept at 0.1 V/nm. Clear MCD inhomogeneities can be seen across the spin-flip transition.

## 6. Temperature dependence of magnetization of bilayer $CrI_3$ (zero electric fields)

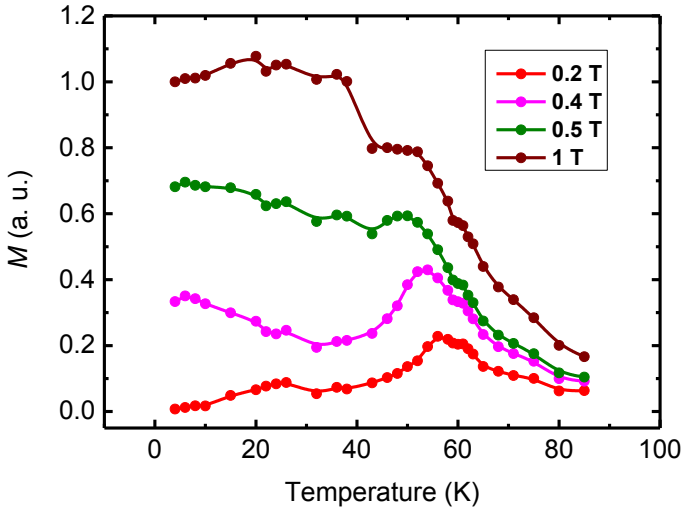


**Figure S7** | Temperature dependence of magnetization of bilayer $CrI_3$ (device #1) under different magnetic fields and zero electric field.

Figure 1d of the main text shows the MCD signal, or equivalently, magnetization as a function of magnetic field and temperature in a contour plot for bilayer $CrI_3$ device #3. The behavior is similar in other devices. We show the magnetization as a function of temperature at several representative magnetic fields for device #1 in Fig. S7. Near zero magnetic field, upon cooling the magnetization increases, peaks at a critical temperature $T_C$ of ~ 57 K, and decreases quickly with further decrease in temperature. This is a characteristic temperature dependence of the magnetic susceptibility of an antiferromagnet [6], as expected for bilayer $CrI_3$ under small magnetic fields. On the other hand, at large magnetic fields (1 T) the magnetization is largely saturated by the external magnetic field. It increases monotonically as temperature decreases and saturates at low temperature. Such a behavior is typical for a ferromagnet [2, 6], as expected for bilayer $CrI_3$ under high magnetic fields. Finally, at intermediate magnetic fields the behavior is

mixed. There is a magnetic-field dependent temperature (smaller than $T_C$), below which the temperature dependence of the magnetization is antiferromagnet-like and above which ferromagnet-like. Such a behavior is caused by a temperature-driven metamagnetic transition from the ferromagnetic state to the antiferromagnetic state upon cooling. Similar metamagnetic transitions have been observed in other material systems [7] such as $DyPO_4$ [8] and $FeCl_2$ [9].

## 7. Temperature dependence of the spin-flip critical field (zero electric field)

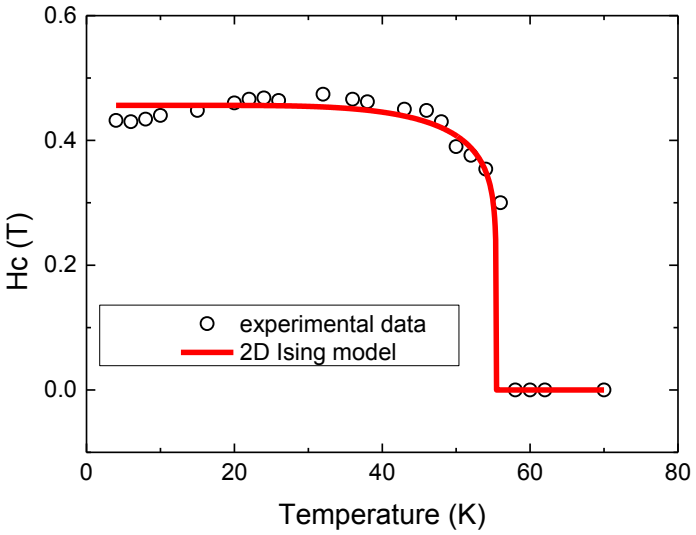


**Figure S8 |** Temperature dependence of the critical magnetic field for the spin-flip transition in bilayer $CrI_3$ (device #3).

Figure S8 shows the critical field $H_C$ (symbols) as a function of temperature. We note that the expression $H_C = \frac{2J+\mu_0 M_0^2/2t}{\mu_0 M_0}$ given in the main text is valid only at zero temperature. It can be modified to take into account the finite temperature effects: the saturation magnetization $M_0$ is replaced by the temperature-dependent magnetization $M(T)$ and the interlayer exchange constant $J$ by $J\left(\frac{M(T)}{M_0}\right)^2$ to count for the decreasing magnetization with increasing temperature. The spin-flip critical field at temperature $T$ is then given by $H_C(T) = M(T)\left(\frac{2J}{\mu_0 M_0^2} + \frac{1}{2t}\right)$, which describes the experimental result well (solid line, Fig. S8). In the fit, we have used the analytical expression of $M(T)$ for the 2D Ising model with a honeycomb lattice [10] and assumed $J$ a constant. The solid line corresponds to $J \approx 30$ μJm$^{-2}$ for device #3. The value extracted from the fit varies slightly from sample to sample. For instance, $J \approx 25$ μJm$^{-2}$ was obtained for device #1.

## 8. Temperature dependence of the magnetoelectric effect in bilayer $CrI_3$

Figure 3 of the main text shows the magnetoelectric (ME) response of bilayer $CrI_3$ under different magnetic fields at 4 K. Figure S9a illustrates the effect at different temperatures. At low temperatures (4 K, 20 K and 30 K), as discussed in the main text, the field-induced change in the magnetization has two values of opposite sign (dependent on the sweeping direction of the magnetic field) in the antiferromagnetic state (i.e. for

$-H_C < H < H_C$). There are also peaks and dips around the critical field $\pm H_C$, providing a way to determine $H_C$. At temperature above $T_C$ (60 K), the ME response is zero as expected based on the symmetry analysis. At intermediate temperature (50 K), the field-induced change in the magnetization still has two values of opposite sign. However, the hysteresis is significantly reduced (almost disappears at temperatures close to $T_C$) and the response switches sign near zero magnetic field. Similar behavior has also been observed in $DyPO_4$ [8].

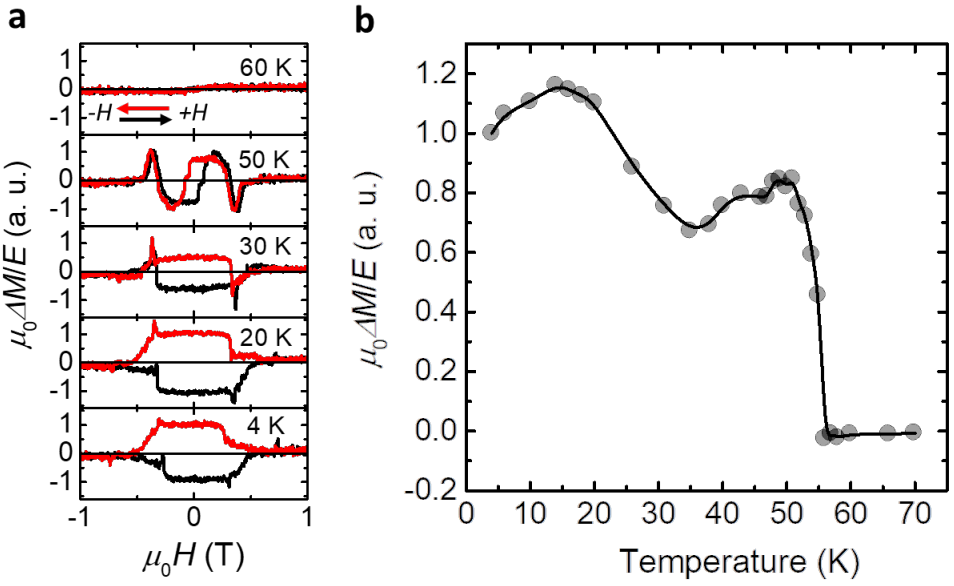


**Figure S9** | **a**, Magnetoelectric response of bilayer $CrI_3$ as a function of magnetic field at different temperatures. **b**, Temperature dependence of the magnetoelectric response at zero magnetic field (symbols). The black solid line is a guide to the eye.

To understand the temperature-dependent hysteresis, we note that the ME effect contributes a term of $-\alpha_{zz}EH$ to the total free energy of the system [11, 12], where $\alpha_{zz}$ is a linear ME coefficient, as discussed in the main text. The ME coefficient can take two values of opposite sign, corresponding to two distinct AFM configurations [8, 13, 14]. For the $\alpha_{zz} < 0$ configuration, if $H < 0$ and $E > 0$, the ME term is negative and lowers the total free energy of the system, i.e. the electric field leads to an energetically more favorable state. As the magnetic field increases and changes sign ($H > 0$), the configuration with $\alpha_{zz} < 0$ is no longer favored because now the energy term $-\alpha_{zz}EH$ is positive. Similar arguments can be made for the $\alpha_{zz} > 0$ configuration. The observation that $\alpha_{zz}$ exhibits a robust hysteresis and does not immediately change sign across $\mu_0 H = 0$ T at low temperature suggests that there is an energy barrier for switching the AFM configurations in bilayer $CrI_3$. Only at high enough magnetic fields the energy barrier is overcome and $\alpha_{zz}$ switches sign. At elevated temperatures, however, thermal excitations across the energy barrier become efficient so that the hysteresis is significantly weakened. Finally, at high enough temperature, almost no hysteresis is seen and $\alpha_{zz}$ changes sign abruptly across $\mu_0 H = 0$ T, reflecting the fact that the system relaxes to the energetically more favorable state immediately. The origin of the energy

barrier is unclear at this stage. Plausible mechanisms include strong out-of-plane magnetic anisotropy [9] and energy barriers for domain wall motions.

We summarize the magnitude of the ME response of bilayer $CrI_3$ at zero magnetic field as a function of temperature in Fig. S9b. The contrast between the AFM and FM state is very clear. The relatively small non-monotonic variation of the ME response as a function of temperature, however, may have a significant contribution from the measurement artifact considering the large sample inhomogeneities and the temperature stability of the optical setup over a large temperature range (4 - 60 K).

## 9. Magnetoelectric annealing in bilayer $CrI_3$

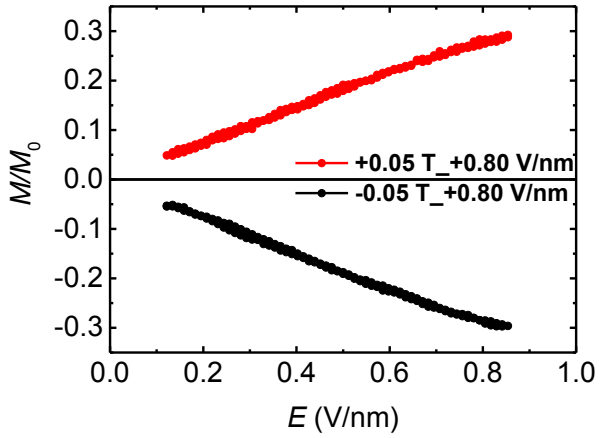


**Figure S10** | Normalized magnetization versus applied electric field for bilayer $CrI_3$ at 4 K under zero magnetic field. The sample has been cooled to 4 K from above $T_C$ under a combination of the electric and magnetic fields.

As discussed above in Sect. 8 and in the main text, the ME effect contributes a term $-\alpha_{zz}EH$ to the free energy of bilayer $CrI_3$ in the AFM state [11, 12]. For a given AFM configuration (i.e. a given sign of $\alpha_{zz}$), the product $EH$ determines the sign of the ME free energy. Reversely, it is possible to control the sign of $\alpha_{zz}$ or the AFM configuration by controlling the sign of $EH$ or the ME free energy, a process known as ME annealing [14]. Figure S10 illustrates this concept. When the sample is cooled from above the critical temperature $T_C$ to 4 K under simultaneous application of an electric field and a magnetic field with $EH > 0$ (red symbols), the sample makes a transition to the AFM state with $\alpha_{zz} > 0$ to minimize the total free energy of the system. This is experimentally verified from the positive slope of the electric-field dependence of the magnetization near zero magnetic field. Similarly, when the sample is cooled under $EH < 0$, the ME coefficient $\alpha_{zz}$ is negative.

## 10. Extra data on electrical switching of magnetic order in bilayer $CrI_3$

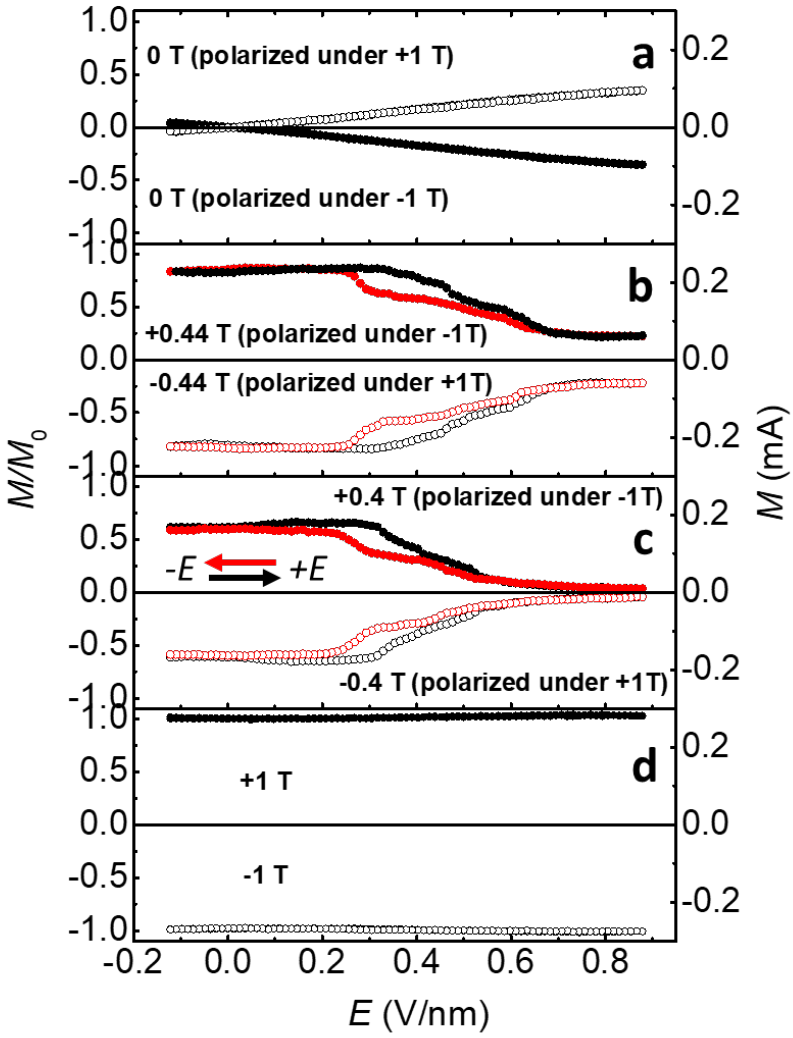


**Figure S11 |** Normalized magnetization as a function of applied electric field in bilayer $CrI_3$ at 4 K under a magnetic field of ± 0 T (**a**), ± 0.44 T (**b**), ± 0.4 T (**c**) and ± 1 T (**d**).

## 11. Magnetoelectric effect in extra bilayer $CrI_3$ devices

We have studied in total three different bilayer $CrI_3$ devices. All of them show similar results. In addition to the data from device #1 presented in the main text, the major results of the other two devices are summarized in Fig. S12. These results demonstrate the robustness of the ME effect. Furthermore, all three devices show similar magnetic-field dependence of the ME susceptibility except the detailed features near the spin-flip transition, where different inhomogeneities in different samples give rise to slightly different features.

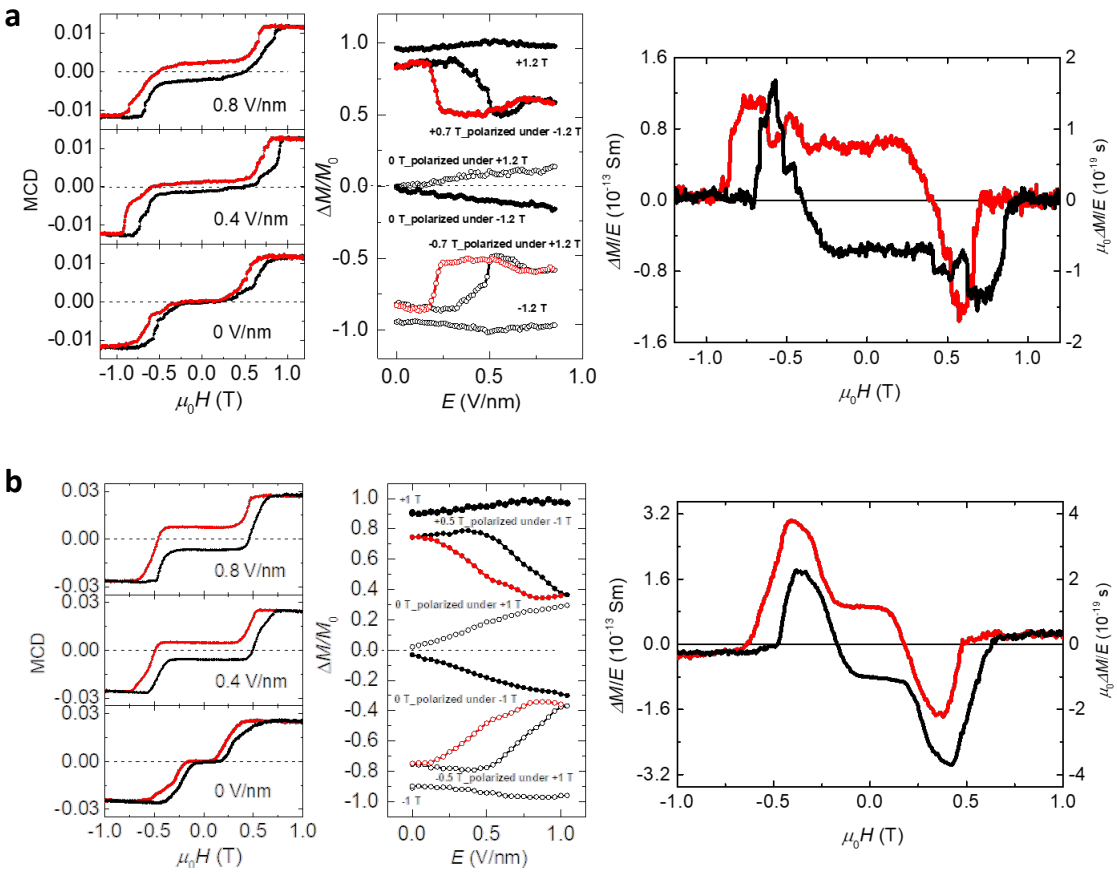


**Figure S12 |** ME effect (left column) and electrical switching of magnetic order (middle column) in bilayer $CrI_3$ device #2 (**a**) and device #3 (**b**). The magnetic field dependence of the sheet ME coefficient (right column) is also shown for each device.

## 12. Spin-dependent interlayer charge transfer model for the ME effect in bilayer $CrI_3$

We estimate the magnitude of the ME coefficient for AFM $CrI_3$ bilayers based on the spin-dependent interlayer charge transfer model as discussed in the main text. First, we consider a parallel plate capacitor model to derive the interlayer charge density difference $\Delta n$ in bilayer $CrI_3$ under a gate voltage difference $\Delta V_g$ between the top and bottom gates in a dual-gate device (Fig. S13). Bilayer $CrI_3$ has an interlayer distance $t$ and a dielectric constant $\varepsilon_c$ (the out-of-plane dielectric constant of $CrI_3$). The symmetric top and bottom gate dielectric have a thickness $d$ and a dielectric constant $\varepsilon$ (the out-of-plane dielectric constant of hBN). Field $F_g$ and $F_c$ denote the vertical electric fields in the gate dielectric and in bilayer $CrI_3$, respectively. The positive direction is chosen to be along the arrows pointing from bottom to top. An interlayer charge imbalance $\Delta n = 2n$ is created under the influence of $\Delta V_g$ ($n$ is the carrier density transferred from one layer to the other).

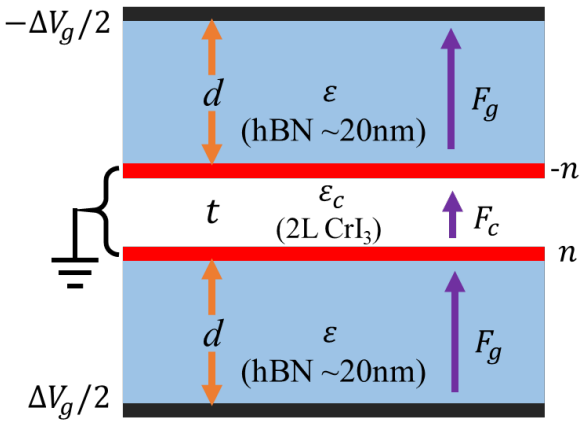


**Figure S13** | Schematic of a dual-gated bilayer $CrI_3$ device.

We can relate the vertical electric fields to the sheet carrier densities at the two $CrI_3$ layers by matching the boundary conditions

$$\begin{aligned} -ne &= -\varepsilon\varepsilon_0 F_g + \varepsilon_c\varepsilon_0 F_c \\ ne &= -\varepsilon_c\varepsilon_0 F_c + \varepsilon\varepsilon_0 F_g. \end{aligned} \tag{S1}$$

Here $e$ is the elementary charge. We can also relate the electrostatic fields to the electrochemical and chemical potentials of the various plates of the capacitors:

$$F_g \approx \frac{\Delta V_g - \Delta E_f/e}{2d}, \qquad F_c = \frac{\Delta E_f}{et}. \tag{S2}$$

Here $\Delta E_f = \frac{\Delta n e^2}{C_q}$ is the Fermi energy difference between the bottom and top $CrI_3$ layer. It is related to the quantum capacitance of each monolayer, $C_q = \frac{2m^* e^2}{\pi\hbar^2}$, where $m^*$ and $\hbar$ denote the band mass and the Planck's constant, respectively. Due to the heavy band mass in $CrI_3$ [15], energy $\Delta E_f$ is negligible compared to $e\Delta V_g$.

Now we combine Eqns. (S1) and (S2) to relate $\Delta n$ to $\Delta V_g$:

$$\Delta ne = \frac{C_q C_g}{C_q + 2C_c + C_g}\Delta V_g \approx C_g \Delta V_g. \tag{S3}$$

Here $C_g = \frac{\varepsilon\varepsilon_0}{d}$ and $C_c = \frac{\varepsilon_c\varepsilon_0}{t}$ are the geometric capacitance of the gates and bilayer $CrI_3$, respectively, and $\varepsilon_0$ is the vacuum permittivity. In the derivation we have considered that the relevant capacitances differ by orders of magnitude: $C_q >> C_c >> C_g$ because of the heavy band mass of $CrI_3$ [15] and $d \gg t$. With Eqn. (S3) we arrive at the relation for the equivalent volumetric ME coefficient

$$\alpha_{zz} \equiv \frac{\mu_0 \Delta M}{2tE} = \frac{\mu_0(\Delta n \mu_B)}{2tE} \approx \frac{2\varepsilon\mu_B}{2tec^2}, \tag{S4}$$

where the applied electric field is given by the gate voltage $E = \Delta V_g/2d$, and $\mu_0$ and $c$ denote the vacuum permeability and speed of light in vacuum, respectively. In Eqn. (S4) we have assumed each transferred electron carry a magnetic moment of Bohr magneton $\mu_B$. Using $\epsilon \approx 3$ for the dielectric constant of hBN [16, 17] and $t \approx 0.7$ nm [2, 3], an equivalent volumetric magnetoelectric coefficient of $\alpha_{zz} \sim 10$ ps/m was estimated.

**13. Data on monolayer $CrI_3$**

Figure S14a shows the out-of-plane magnetic-field dependence of the MCD signal and the calibrated sheet magnetization of monolayer $CrI_3$. The behavior is completely different from that of bilayer $CrI_3$ (Fig. 1c of the main text), in which the dependence is dominated by a spin-flip transition from the interlayer antiferromagnetic state to the bilayer ferromagnetic state at the critical field $H_C \approx 0.5$ T. For monolayer $CrI_3$ a characteristic ferromagnetic dependence with strong out-of-plane anisotropy and small coercive field (~ 0.1 T) is seen. The result is consistent with a recent study [4]. Figure S14b is the ME response of monolayer $CrI_3$, which is the same data as shown in Fig. 3 of the main text. The response is more than 100 times smaller than the response in bilayer $CrI_3$. The presence of a tiny linear magnetoelectric effect in monolayer $CrI_3$ is not expected based on symmetry analysis [18, 19]. A possible reason is the presence of a nonzero built-in electric field (as seen in bilayers) that breaks the inversion symmetry.

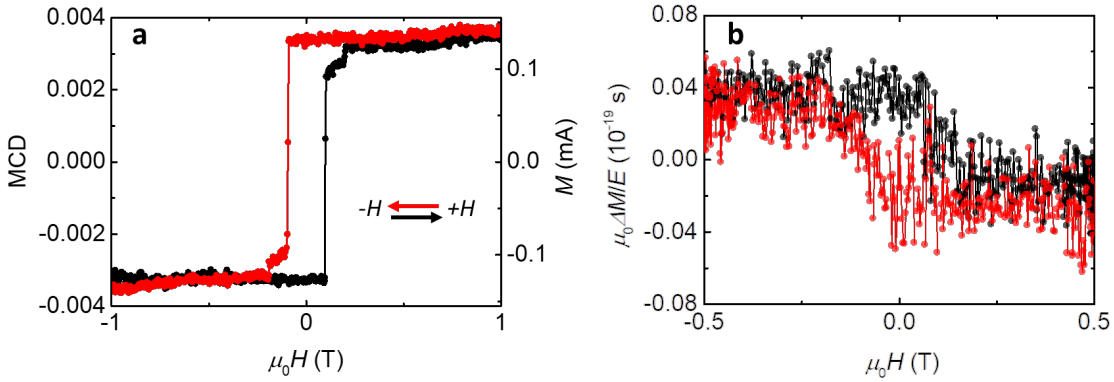


**Figure S14 | a,** Hysteresis loop of the MCD signal (left axis) and sheet magnetization (right axis) as a function of applied out-of-plane magnetic field for monolayer $CrI_3$ at 4 K. **b,** ME response of monolayer $CrI_3$ at 4 K obtained by subtracting *M-H* curves under 0.34 V/nm and - 0.34 V/nm.

## References


1. Zhang, W.-B., Qu, Q., Zhu, P. & Lam, C.-H. Robust intrinsic ferromagnetism and half semiconductivity in stable two-dimensional single-layer chromium trihalides. *Journal of Materials Chemistry C* **3**, 12457-12468 (2015).
2. McGuire, M.A., Dixit, H., Cooper, V.R. & Sales, B.C. Coupling of Crystal Structure and Magnetism in the Layered, Ferromagnetic Insulator CrI3. *Chemistry of Materials* **27**, 612-620 (2015).
3. McGuire, M.A. Crystal and Magnetic Structures in Layered, Transition Metal Dihalides and Trihalides. *Crystals* **7**, 121 (2017).
4. Huang, B., Clark, G., Navarro-Moratalla, E., Klein, D.R., Cheng, R., Seyler, K.L., Zhong, D., Schmidgall, E., McGuire, M.A., Cobden, D.H., Yao, W., Xiao, D.,

Jarillo-Herrero, P. & Xu, X. Layer-dependent ferromagnetism in a van der Waals crystal down to the monolayer limit. *Nature* **546**, 270-273 (2017).
5. Miyake, A., Sato, Y., Tokunaga, M., Jatmika, J. & Ebihara, T. Different metamagnetism between paramagnetic Ce and Yb isomorphs. *Physical Review B* **96**, 085127 (2017).
6. Jiles, D. *Introduction to magnetism and magnetic materials* (Taylor & Francis Group, Boca Raton, 2016).
7. Kimura, T. Spiral Magnets as Magnetoelectrics. *Annual Review of Materials Research* **37**, 387-413 (2007).
8. Rado, G.T. Magnetoelectric Evidence for the Attainability of Time-Reversed Antiferromagnetic Configurations by Metamagnetic Transitions in DyPO4. *Physical Review Letters* **23**, 644-647 (1969).
9. Jacobs, I.S. & Lawrence, P.E. Metamagnetic Phase Transitions and Hysteresis in FeCl2. *Physical Review* **164**, 866-878 (1967).
10. Naya, S. On the Spontaneous Magnetizations of Honeycomb and Kagomé Ising Lattices. *Progress of Theoretical Physics* **11**, 53-62 (1954).
11. Eerenstein, W., Mathur, N.D. & Scott, J.F. Multiferroic and magnetoelectric materials. *Nature* **442**, 759-765 (2006).
12. Manfred, F. Revival of the magnetoelectric effect. *Journal of Physics D: Applied Physics* **38**, R123 (2005).
13. Rado, G.T. Mechanism of the Magnetoelectric Effect in an Antiferromagnet. *Physical Review Letters* **6**, 609-610 (1961).
14. Borisov, P., Hochstrat, A., Chen, X., Kleemann, W. & Binek, C. Magnetoelectric Switching of Exchange Bias. *Physical Review Letters* **94**, 117203 (2005).
15. Wang, H., Eyert, V. & Schwingenschlögl, U. Electronic structure and magnetic ordering of the semiconducting chromium trihalides CrCl 3 , CrBr 3 , and CrI 3. *Journal of Physics: Condensed Matter* **23**, 116003 (2011).
16. Fallahazad, B., Movva, H.C.P., Kim, K., Larentis, S., Taniguchi, T., Watanabe, K., Banerjee, S.K. & Tutuc, E. Shubnikov-de Haas Oscillations of High-Mobility Holes in Monolayer and Bilayer WSe2: Landau Level Degeneracy, Effective Mass, and Negative Compressibility. *Physical Review Letters* **116**, 086601 (2016).
17. Wang, Z., Shan, J. & Mak, K.F. Valley- and spin-polarized Landau levels in monolayer WSe2. *Nat Nano* **12**, 144-149 (2017).
18. Cracknell, A.P. *Magnetism in Crystalline Materials: Applications of the Theory of Groups of Cambiant Symmetry* (Pergamon Press, New York, 1975).
19. Sivadas, N., Okamoto, S. & Xiao, D. Gate-Controllable Magneto-optic Kerr Effect in Layered Collinear Antiferromagnets. *Physical Review Letters* **117**, 267203 (2016).